

RESEARCH ARTICLE

Study on the changes of extracellular matrix morphology and components in COPD animal model by using lung decellularized scaffold

Yuan Li¹  | Yingbing Dai²  | Ting Jin¹  | Xianyang Liu¹  | Lihua Xie¹ 

¹Department of Pulmonary and Critical Care Medicine, The Third Xiangya Hospital of Central South University, Changsha, China

²Department of Internal Medicine, Hunan Provincial Chest Hospital, Changsha, China

Correspondence

Lihua Xie, Department of Pulmonary and Critical Care Medicine, The Third Xiangya Hospital of Central South University, Changsha 410013, China.
Email: xyelyhua@163.com

Funding information

MOST | National Natural Science Foundation of China (NSFC), Grant/Award Number: 82070048; HSTD | Natural Science Foundation of Hunan Province (湖南省自然科学基金), Grant/Award Number: 2023JJ30849; CSU | Fundamental Research Funds for Central Universities of the Central South University (Fundamental Research Funds for the Central Universities of Central South University), Grant/Award Number: 1053320231385 and 1053320230888

Abstract

Airway remodeling is a critical pathological process that influences the progression of chronic obstructive pulmonary disease (COPD). To better study small airway remodeling in COPD, we employed advanced techniques such as decellularized scaffolds, immunofluorescence, scanning electron microscopy, and proteomics to analyze morphological and compositional changes in the extracellular matrix (ECM). Our study revealed significant ultrastructural abnormalities in the decellularized scaffolds from the COPD group, including thinning of alveolar septa, enlargement of alveolar spaces, and fusion of multiple alveoli. Additionally, the ECM composition in the COPD group exhibited notable changes characterized by an increase in collagen fibers, type I and IV collagens, fibronectin, and laminin ($p < .05$), along with a decrease in elastin and glycosaminoglycans ($p < .05$). Proteomic analysis identified 70 differentially expressed proteins between the COPD group and the control group. These included 34 upregulated proteins such as Smarca2, Skt, Acvr11, Myl2 (all with ratios >10.64), and 36 downregulated proteins such as Col6a6, Col6a5, and AnK3 (all with ratios <0.27). Pathway analysis indicated that activation of apoptosis (Enrichment Score, ES = 0.23) and epithelial–mesenchymal transition (ES = 0.38) genes and inhibition of collagen synthesis (ES = -0.43) and degradation (ES = -0.63) genes were observed in the COPD group. These findings enhance our understanding of the mechanisms underlying airway remodeling and provide a scientific basis for developing novel therapeutic strategies for COPD.

KEYWORDS

airway remodeling, collagen, COPD (chronic obstructive pulmonary disease), ECM (extracellular matrix), lung decellularized scaffolds, proteomics

This is an open access article under the terms of the [Creative Commons Attribution-NonCommercial-NoDerivs](https://creativecommons.org/licenses/by-nc-nd/4.0/) License, which permits use and distribution in any medium, provided the original work is properly cited, the use is non-commercial and no modifications or adaptations are made.

© 2025 The Author(s). *The FASEB Journal* published by Wiley Periodicals LLC on behalf of Federation of American Societies for Experimental Biology.

1 | INTRODUCTION

Chronic Obstructive Pulmonary Disease (COPD) is a leading cause of morbidity and mortality worldwide, affecting 13.7% of individuals over 40 years old in China.¹ COPD is characterized by chronic cough, sputum production, difficulty breathing, and persistent airflow obstruction, primarily due to abnormal airway and alveolar structures.² Its pathogenesis involves chronic inflammation, excessive airway mucus secretion, protease–antiprotease imbalance, oxidative stress, cell apoptosis, and small airway remodeling. Small airway remodeling is a critical pathophysiological basis for airflow limitation, yet its mechanisms remain unclear. Currently, there are no treatments targeting airway remodeling in COPD. Therapy mainly consists of anti-inflammatory agents and bronchodilators, which do not effectively reverse disease progression. Therefore, in-depth research into the mechanisms of airway and lung parenchyma remodeling and the exploration of new treatment methods is of great importance for improving patient prognosis.³

Airway remodeling includes goblet cell hyperplasia, proliferation, and hypertrophy of airway smooth muscle cells, subepithelial fibrosis, basement membrane thickening, and extracellular matrix (ECM) collagen deposition.⁴ Lung parenchymal destruction involves alveolar wall thinning, rupture, and fibrosis. All these changes contribute to significant ECM abnormalities. The ECM, beyond providing structural support, also influences cell behavior through biochemical and biomechanical signals. The interstitial matrix forms a fibrous network, maintaining the lung's three-dimensional structure through interconnections between cells and tissues. Key ECM components in the lungs include type IV collagen, laminins, fibrillar collagens, elastin, fibronectin, glycosaminoglycans, and proteoglycans.^{5,6} These substances play a crucial role in maintaining ECM structural integrity and in cell adhesion, migration, proliferation, differentiation, apoptosis, and cytokine secretion.^{7–10} In COPD, increased ECM degradation and abnormal synthesis lead to small airway fibrosis and mucosal thickening, causing luminal narrowing and airflow limitation.^{11,12} However, the changes in the main components of the ECM in COPD and the related mechanisms remain unclear, with little known about abnormalities in its ultrastructure or proteomic composition. Previous studies, mostly involving lung tissues with high cellular content, have posed significant challenges in understanding ECM changes and mechanisms in depth.

To better understand ECM remodeling in COPD, this study employed the lung decellularization scaffold, a technique that removes cellular components while preserving the three-dimensional structure and ECM components.¹³ Decellularization scaffolds have been used in tissue

engineering and regenerative medicine, but their application in COPD pathogenesis remains limited. Previous research shows that COPD lung decellularized scaffolds can induce differential gene expression in epithelial cells¹⁴ and affect the adhesion and growth of bone marrow mesenchymal stem cells,^{15,16} suggesting that diseased lung decellularized scaffolds might impact cell function and interactions. We assessed ECM changes in COPD using scanning electron microscopy, histological staining, and proteomics. By reducing cellular interference, this approach enhances our understanding of airway remodeling mechanisms and identifies potential new drug targets and treatments.

2 | MATERIALS AND METHODS

This study received ethical approval from the Medical Ethics Committee of the Third Xiangya Hospital, Central South University (Approval No. 2020-S171).

2.1 | Building and evaluation of mouse COPD model

In this research, we procured twenty wild-type (WT) C57BL/6 mice, aged between 6 and 8 weeks, from Vital River Laboratory Animal Technology Co., Ltd., Beijing, China. These mice were then randomly assigned into two groups: a control group and a COPD model group. The COPD model was established using a combination of exposure to cigarette smoke (CS) and intraperitoneal injections of cigarette smoke extract (CSE), employing a methodology previously developed and described by our group.¹⁷

In the COPD model group, mice were subjected to cigarette smoke (CS) exposure from 20 cigarettes daily for two sessions each day, totaling 28 days. Additionally, on days 1, 12, and 23, these mice received intraperitoneal injections of a cigarette smoke extract (CSE) solution (0.3 mL/20 g) without concurrent CS exposure. Conversely, the control group mice were kept in an environment with fresh air and received intraperitoneal injections of phosphate-buffered saline (PBS) provided by Servicebio on the same days (1, 12, and 23).

2.2 | Assessment of lung function and histology in COPD animal model

For lung function assessment in this study, a small animal lung function instrument (PLY3211; Buxco Research Systems, Wilmington, NC, USA), provided by Central

South University (Changsha, China), was utilized to measure the lung functions of all participating mice. On the 28th day, mice from both the control group ($n=5$) and the COPD model group ($n=5$) were randomly selected for the measurement of inspiratory/expiratory time ratio (Ti/Te), peak expiratory flow (PEF), airway resistance (Raw), and lung dynamic compliance (Cdyn).¹⁸ Following the lung function assessments, the mice were euthanized. The right middle lobe was excised, fixed in formalin, and subsequently, lung tissue sections were stained with hematoxylin and eosin (H&E) to evaluate histomorphology. Parameters such as the mean linear intercept (MLI) and mean alveolar septal thickness (MAST) were measured by a pathologist who was blinded to the groups. The efficacy of the model was evaluated based on pulmonary function tests and histopathological alterations in the lungs.

2.3 | Preparation and evaluation of lung decellularized scaffolds

Isolated pulmonary perfusion was carried out using the Langendorff perfusion system through the pulmonary artery, employing apparatus from Zhongshi Science & Technology, China. For this purpose, both the control group ($n=5$) and the COPD model group ($n=5$) were utilized to fabricate lung decellularized scaffolds. This was achieved by vascular perfusion with a solution of polyethylene glycol octyl phenyl ether (Triton X-100, Sigma, diluted to 1:100) and sodium dodecyl sulfate (SDS, Sigma, diluted to 8:1000).¹⁹ Observations of the lung decellularized scaffolds' color and morphological changes were made at various time intervals during the decellularization process. Additionally, the DNA concentrations in both fresh lung tissues and lung decellularized scaffolds from the COPD model groups were quantified using the Universal Column Genomic DNA Kit (cwbio, China).

2.4 | Changes of composition and ultrastructure of lung decellularized scaffold

The lung decellularized scaffolds from both the control and COPD model groups were embedded into paraffin wax blocks, sectioned, and then subjected to various staining methods to observe the morphological and compositional changes of different components. Hematoxylin and eosin (H&E) staining, Masson's trichrome staining, Elastica van Gieson (EVG) staining, and Alcian blue staining were performed using kits provided by Servicebio, China. Immunofluorescence staining was utilized to examine alterations in the morphology and abundance of collagen I

(Col I), collagen IV, fibronectin (FN), and laminin (LN) in the sections. Furthermore, scanning electron microscopy (ZEISS, Germany) was employed to assess the ultrastructural modifications of the scaffolds.

2.5 | Label-free quantitative proteomics analysis

2.5.1 | Protein extraction and quantification

Lung decellularized scaffold samples from the COPD group ($n=3$) and the control group ($n=2$) were placed in tubes containing SDT lysis buffer. The samples were then homogenized using an MP homogenizer (MP Fastprep-245G, USA) and centrifuged. The supernatant was filtered through a 0.22- μm centrifuge tube. Protein quantification was conducted using the BCA method, and the samples were aliquoted and stored at -80°C .

2.5.2 | Protein separation and filter-aided sample preparation (FASP) digestion

For each sample, 20 μg of protein was taken, mixed with loading buffer (Beyotime, China), heated, and then subjected to SDS-PAGE electrophoresis. After Coomassie Brilliant Blue staining, 100 μg of protein was processed, treated with DTT (Sigma, USA) and UA buffer (BIO-RAD, USA) for centrifugation. The samples were then reacted with IAA buffer in the dark, followed by centrifugation and two additional centrifugations with UA buffer. After that, NH_4HCO_3 solution (Sigma, USA) was added and centrifuged. The samples were incubated with trypsin buffer, centrifuged, desalted using a C18 Cartridge (Waters, USA), lyophilized, resuspended in formic acid solution (Thermo Fisher Scientific, USA), and finally, the peptide segments were quantified. The mass spectrometry analysis and data processing followed.

The samples were separated using the NanoElute system (Bruker, Bremen, Germany), with a 0.1% formic acid aqueous solution (Thermo Fisher Scientific, USA) and a 0.1% formic acid acetonitrile aqueous solution (Merck, USA) as the buffer, and separated through a C18 analytical column (IonOpticks, Australia). Mass spectrometry analysis was conducted using the timsTOF Pro mass spectrometer (Bruker, Bremen, Germany) in PASEF mode, with a total duration of 90 min. The precursor ion scan range was set to 100–1700 m/z , with an ion mobility range of 0.75–1.4 $\text{V}\cdot\text{s}/\text{cm}^2$. The capillary voltage was set at 1500V, with a drying gas flow rate of 3L/min and a temperature of 180°C . PASEF settings included 10 MS/MS scans with an ion target intensity of 10,000, among other parameters. Lastly, protein identification was conducted using the UniProt database.

2.6 | Bioinformatics analysis

Through the Blast2GO software, we annotated the proteins with GO functions, involving four steps: sequence alignment, GO term retrieval, annotation, and supplementary annotation. Subsequently, the KOALA software was used for KEGG pathway annotation of the target proteins, which included classifying the protein sequences into KO categories and obtaining pathway information. This was followed by enrichment analysis of GO and KEGG annotations, employing Fisher's exact test to compare the distribution of GO terms or KEGG pathways between the target protein set and the overall protein set. Additionally, protein-protein interaction networks were explored using the String database. Finally, GSEA (Gene Set Enrichment Analysis) was conducted on data where at least half of the sample groups had nonnull values, using datasets from the official GSEA website.

2.7 | Statistical analysis

Quantitative processing of images was conducted using ImageJ, and the data obtained were analyzed using SPSS statistical software version 22.0. The comparison of parameters between the control and experimental groups was performed using variance analysis. Quantitative data with a normal distribution were expressed as mean \pm standard deviation, and differences were considered statistically significant at $p < .05$. Mass spectrometry results were processed utilizing the MaxQuant program, version 1.6.17.0. The spectral data were matched against a project-defined database. A threshold of 0.01 was applied for the overall false discovery rate (FDR) in the identification of peptides and proteins. The quantity of proteins was determined from the normalized spectral count intensity (LFQ intensity). Proteins exhibiting a fold change greater than 2 or less than 0.5, along with a p -value from Student's t -test of less than .05, were identified as differentially regulated proteins.

3 | RESULTS

3.1 | Preparation, identification, and morphological changes of COPD lung decellularized scaffold

We prepared and evaluated the morphological changes in the COPD animal model. In the COPD model group, lung tissue sections stained with hematoxylin and eosin (H&E) revealed inflammatory cell infiltration, enlarged alveolar cavities, thinned alveolar septa, fractured alveolar walls, and fusion of multiple alveolar cavities (Figure 1A).

Compared to the control group, the mean linear intercept (MLI) in the COPD model group was increased, whereas the mean alveolar septal thickness (MAST) was decreased (Figure 1B and Table 1, $p < .05$). Furthermore, the COPD group exhibited pulmonary dysfunction, as evidenced by an increase in airway resistance (Raw) and decreases in the inspiratory/expiratory time ratio (Ti/Te), lung dynamic compliance (C_{dyn}), and peak expiratory flow (PEF) compared with the control group (Figure 1C and Table 2, $p < .05$).

We monitored the decellularization process of lung tissue specimens from both the control and the COPD model groups, noting changes in appearance and morphology. Initially, the fresh lungs of both groups were reddish due to the presence of a large number of blood cells. As the detergent perfusion continued, the color of the fresh lungs transitioned from milky white to a white translucent state. Morphologically, the COPD model group's lungs were slightly larger than those of the control group, exhibiting a looser structure and an uneven surface. Volume changes in the lung decellularized scaffolds were observed in both groups, with the lungs initially expanding then gradually shrinking during the perfusion process, ultimately becoming slightly larger than the fresh lungs (Figure 1D). DNA content analysis and H&E staining were employed to verify complete decellularization in the COPD model group's lung decellularized scaffolds. The DNA content in the decellularized scaffolds was significantly lower than that of the control group (39.53 ± 3.60 ng/mg vs. 112.33 ± 10.14 ng/mg) ($p < .01$) (Figure 1E); no cellular or nuclear structures were detected in the lung tissue of either group (Figure 1F), and DNA electrophoresis bands were noticeably fainter (Figure 1G), confirming the successful preparation of the lung decellularized scaffolds. Further examination of lung decellularized scaffold sections from both the control group and the COPD model group via scanning electron microscopy (SEM) showed no residual cells within the scaffolds of either group. In the control group, the ultrastructural network of the lung decellularized scaffolds remained intact and orderly; whereas, in the COPD model group, the structure was severely damaged, the arrangement disordered, the alveolar spaces enlarged, and the thickness reduced (Figure 2).

3.2 | Composition changes in lung decellularized scaffolds between the COPD model group and the control group

Compared to the control group, H&E staining of the lung decellularized scaffolds in the COPD model group revealed enlarged alveolar spaces, thinning of the alveolar

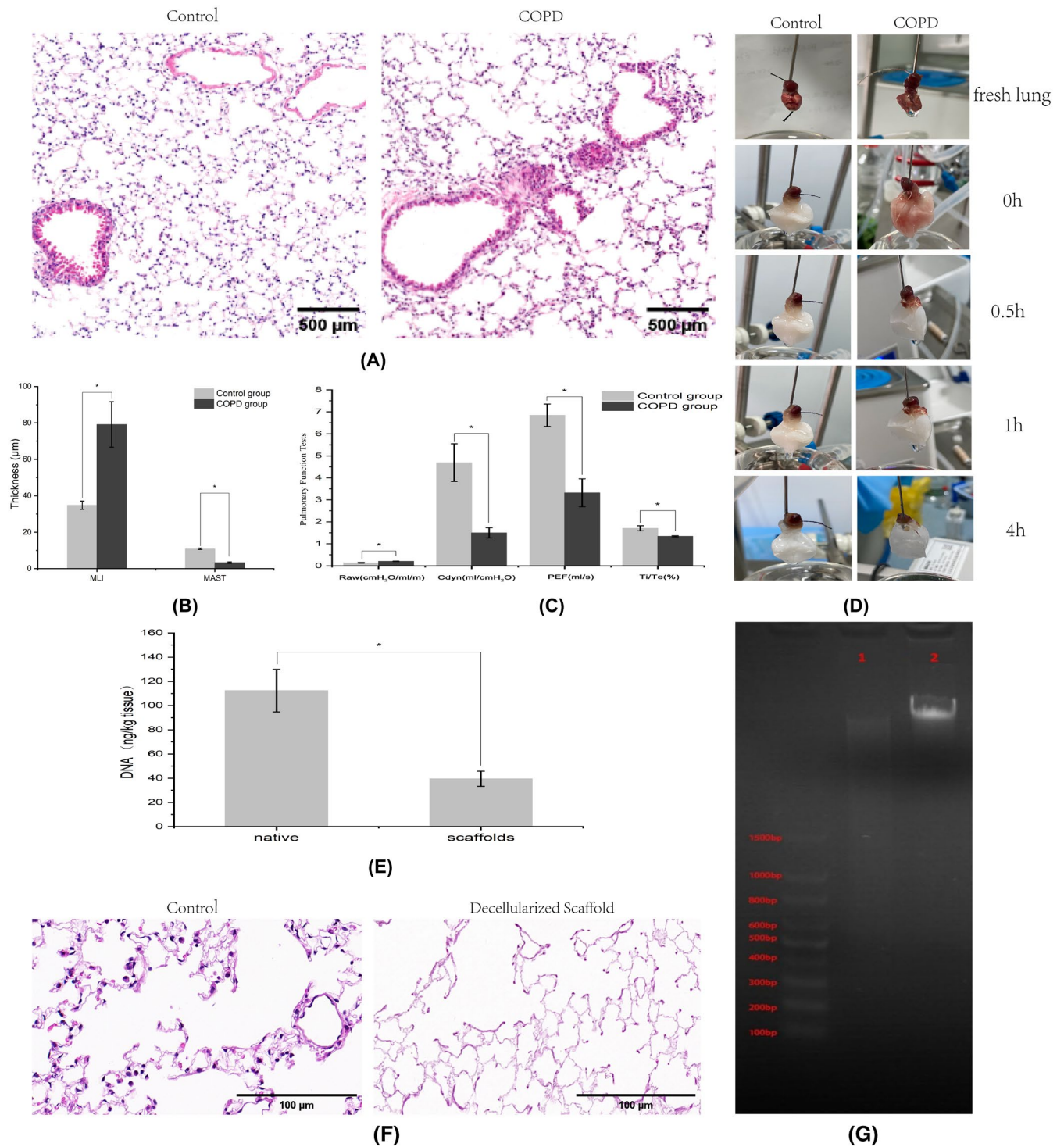


FIGURE 1 Preparation, identification, and morphological changes of lung decellularized scaffold. (A) Paraffin-embedded lung tissue sections from the control and COPD model groups were stained with hematoxylin and eosin (H&E) (100× magnification). (B) Morphometric comparison of Mean Linear Intercept (MLI) and Mean Alveolar Septal Thickness (MAST) between control and COPD model groups. (C) Lung function comparison between control and COPD model groups, including measurements of Airway Resistance (Raw), Lung Dynamic Compliance (Cdyn), Peak Expiratory Flow (PEF), and the Inspiratory/Expiratory Time Ratio (Ti/Te). (D) Changes in lung tissue appearance before starting decellularization, after PBS wash, and at different time points during decellularization. (E) The DNA content in fresh lung tissue (native) and lung decellularized scaffolds of the COPD model group ($n=3$). (F) H&E staining of fresh lung tissue and lung decellularized scaffolds from the COPD model group (magnification 400×). (G) DNA electrophoresis showing (1) fresh lung tissue and (2) lung decellularized scaffolds from the COPD model group. Data are presented as mean \pm standard deviation ($\bar{X} \pm s$), with $*p < .05$ indicating statistical significance. $n = 5$ for each group.

septa, destruction of the alveolar walls, and fusion of multiple alveolar spaces. Masson staining highlighted the deposition of collagen fibers with a mismatched arrangement and disordered structure. Verhoeff–Van Gieson (VG) staining indicated a decrease in the area of elastic fibers with a disordered structure and significant destruction of elastin. Alcian blue staining demonstrated a reduced area of glycosaminoglycan staining and severe disruption of glycosaminoglycans (Figure 3A). Immunofluorescence staining identified the structural ECM proteins Collagen I, Collagen IV, and the elastic ECM proteins Fibronectin and Laminin, all labeled in red (Figure 3B). Semiquantitative analysis using Image J software revealed an increase in the proportion of collagen fibers, a decrease in the proportion of elastic fibers and glycosaminoglycans, and an increased average fluorescence intensity of Collagen I, Collagen IV, Fibronectin, and Laminin ($p < .05$) (Tables 3 and 4, Figure 3C,D).

3.3 | Bioinformatics analysis reveals proteomic differences in lung decellularized scaffold: results from KEGG, GO, PPI, and GSEA analyses

In this study, a total of 3163 proteins were identified and quantified between the COPD and control groups. Differential expression of proteins was screened using a fold change (FC) ≥ 2.0 and $p < .05$ as criteria. Compared to the control group, 70 differentially expressed proteins were found, including 34 upregulated proteins such as Dock9, Smarca2, Rrbp1, Acvr11, Myl2 (all with ratios > 10.64), and 36 downregulated proteins such as Ppl, Col6a6, Col6a5, and Myh1 (all with ratios < 0.27). The top

TABLE 1 Comparison of morphological changes in lung tissue between control and COPD model group ($X \pm s$). Morphometric measurements of MAST (μm) and MLI (μm) were performed in each group.

Group	MLI (μm)	MAST (μm)
Control	34.84 \pm 2.25	10.87 \pm 0.36
COPD	79.17 \pm 12.50*	3.31 \pm 0.41*

* $p < .05$ versus control group ($n = 5$).

TABLE 2 Comparison of lung function between control and COPD model group ($X \pm s$). Comparison measurements of Raw ($\text{cmH}_2\text{O}/\text{mL}/\text{m}$), Cdyn ($\text{mL}/\text{cmH}_2\text{O}$), PEF (mL/s), and Ti/Te (%) were performed in each group.

Group	Raw ($\text{cmH}_2\text{O}/\text{mL}/\text{m}$)	Cdyn ($\text{mL}/\text{cmH}_2\text{O}$)	PEF (mL/s)	Ti/Te (%)
Control	0.14 \pm 0.01	4.69 \pm 0.85	6.84 \pm 0.51	1.71 \pm 0.11
COPD	0.21 \pm 0.00*	1.50 \pm 0.22*	3.32 \pm 0.64*	1.34 \pm 0.03*

* $p < .05$ versus control group ($n = 5$).

10 significantly upregulated and downregulated proteins are shown in Figure 4A.

GO and KEGG enrichment analyses were performed on the upregulated and downregulated proteins, as shown in Figure 4B–E. These analyses were conducted to compare the functional changes between the COPD and control groups. Notably, functions such as carnitine O-acyltransferase activity (FDR = 0.14) and regulation of epithelial cell migration (FDR = 0.14) were significantly enriched among the upregulated proteins, while functions including desmosome (FDR = 0.13), actin filament binding (FDR = 0.10), and cell–cell adhesion (FDR = 0.14) were significantly enriched among the downregulated proteins. Pathways such as focal adhesion ($p = .10$) and ECM–receptor interaction ($p = .11$) were also significantly enriched among the downregulated proteins.

The 70 differential proteins were analyzed as target proteins in a direct interaction network, as shown in Figure 4F. Key hub proteins identified include upregulated proteins Ndufs2 (degree = 11), Ndufa9 (degree = 10), Acads (degree = 4), and Myl2 (degree = 4); and downregulated proteins Ttn (degree = 11), Obscn (degree = 6), Ldb3 (degree = 4), and Myh1 (degree = 3).

GSEA results indicated that epithelial–mesenchymal transition genes (ES = 0.38) and apoptosis genes (ES = 0.23) were enriched among upregulated genes, suggesting activation of these genes in the COPD group. Conversely, genes involved in inflammation regulation (ES = -0.14), collagen formation (ES = -0.43), and collagen degradation (ES = -0.63) were enriched among downregulated genes, indicating suppression of these genes in the COPD group (Figure 4G).

4 | DISCUSSION

In this study, we successfully prepared and evaluated the morphological changes in a COPD animal model. Histological analysis revealed significant pathological features in the COPD model group, including inflammatory cell infiltration, enlarged alveolar cavities, thinned alveolar septa, fractured alveolar walls, and the fusion of multiple alveolar cavities. These findings are consistent with the typical hallmarks of COPD, involving chronic inflammation and structural damage to lung tissue.

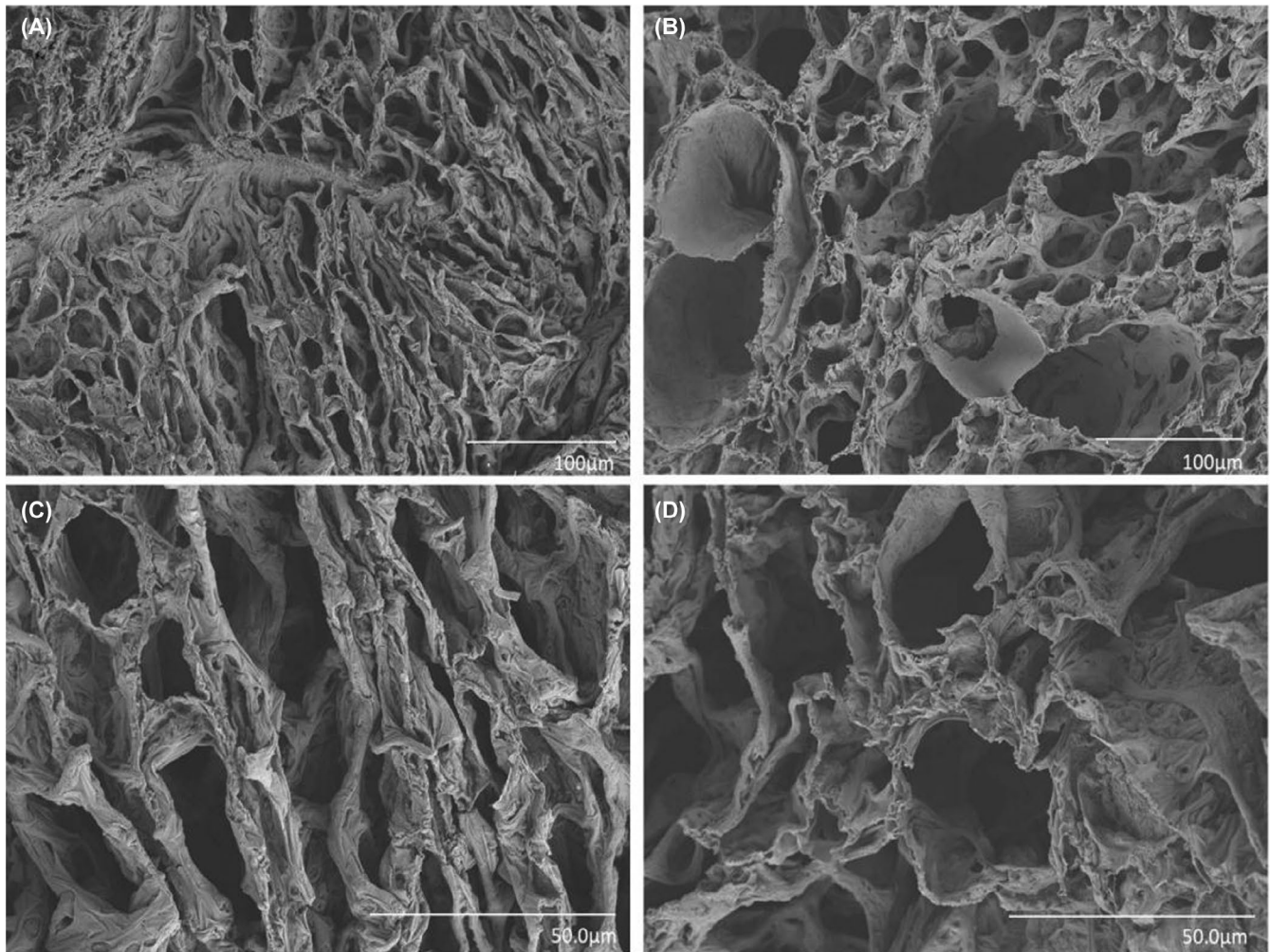


FIGURE 2 Comparison of Lung Decellularized Scaffolds between Control and COPD Model Groups Using SEM. (A) Control group at 300× magnification. (B) COPD model group at 300× magnification. (C) Control group at 500× magnification. (D) COPD model group at 500× magnification. These images reveal that the ultrastructural network of the lung decellularized scaffold in the COPD model group suffered severe damage compared with the control group.

The extracellular matrix (ECM) of the lung forms a complex network of noncellular components that not only provides structural support for lung cells but also directly regulates cell behavior through interactions with cell surface receptors.^{20,21} The ECM plays a crucial role in lung repair and remodeling, significantly influencing the development of lung diseases.⁵ Hoffman et al.'s research further confirmed the critical role of the extracellular matrix (ECM) in chronic lung diseases. They found significant differences in ECM composition across distinct regions of normal lung tissue, such as the alveolar-enriched region, airway region, and vascular region, particularly in collagen and basement membrane-associated proteins.²² These findings are consistent with the results of this study, further highlighting the importance of ECM remodeling in chronic lung diseases. Therefore, investigating ECM changes in the lungs of COPD patients is crucial for disease diagnosis and treatment.

Decellularized scaffolds retain the tissue's three-dimensional structure and ECM components, reducing the interference of cellular components. This enables cell culture and mechanistic studies based on decellularized scaffolds to more accurately simulate the *in vivo* cellular environment and actual disease processes.^{23–26} Compared to traditional planar cultures and Matrigel cultures, this method provides a more realistic biological context.^{27–29} The preparation methods for decellularized scaffolds include physical, chemical, and enzymatic approaches, with chemical decellularization agents being more commonly used.

This study successfully prepared lung decellularized scaffolds that met the criteria set by Crapo et al.,³⁰ as verified by DNA concentration measurements and H&E staining. The lungs of the COPD model exhibited a looser structure and an uneven surface, likely due to extensive damage and remodeling of lung tissue. Scanning

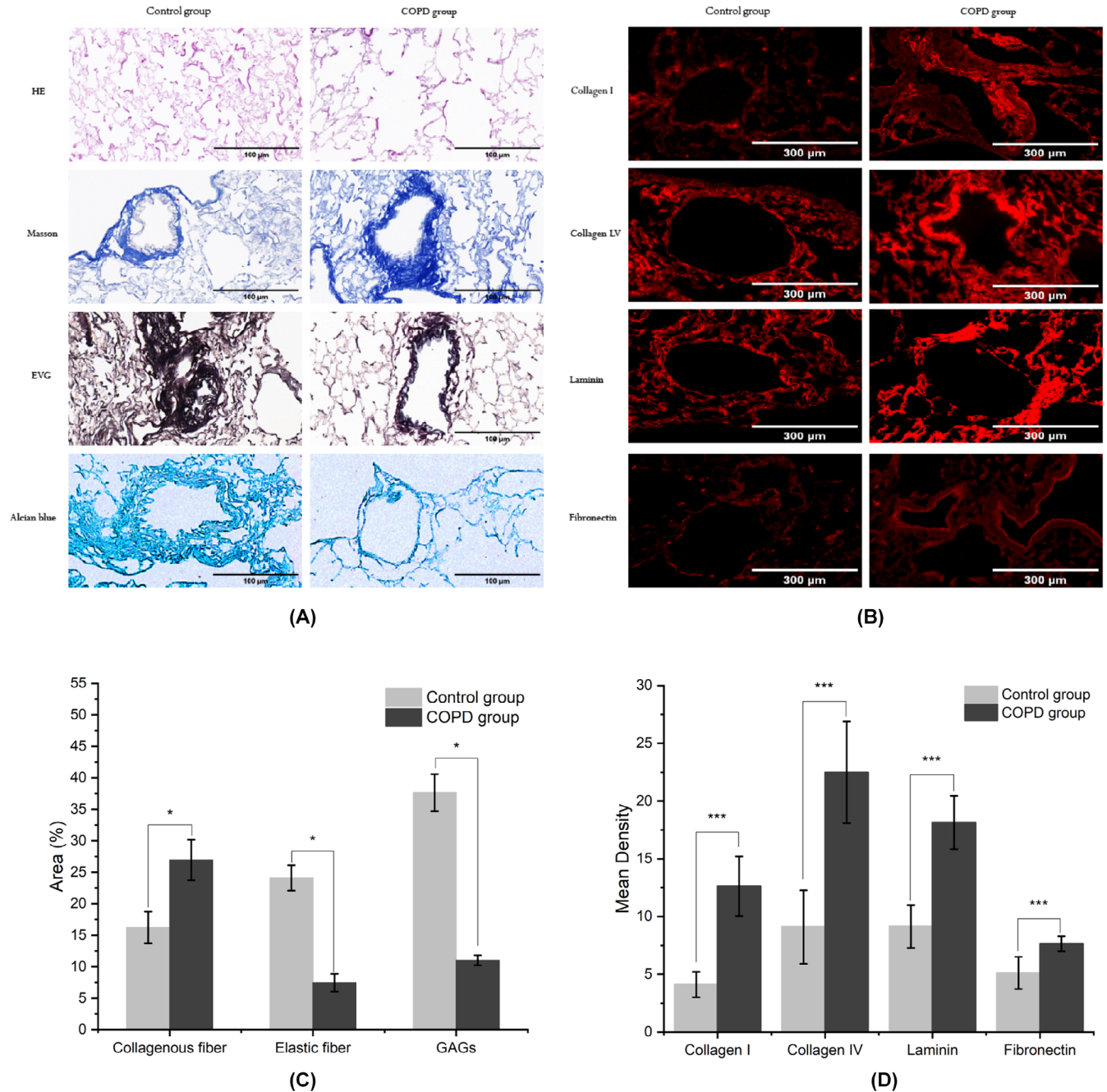


FIGURE 3 Comparison of ECM Components in Lung Decellularized Scaffolds between Control and COPD Model Groups. (A) Analysis of ECM components in lung decellularized scaffolds between the control and COPD model groups (400 \times magnification). H&E staining revealed no residual cells within the alveolar cavities or septa in both groups. Masson staining depicted collagen fibers in blue for both groups, without the presence of blue-brown nuclei or red cytoplasm. EVG staining highlighted elastic fibers in blue-black for both groups, absence of black nuclei and red cytoplasm. Alcian blue staining indicated glycosaminoglycans stained blue in both groups. (B) Immunofluorescence staining for four ECM proteins (Collagen I, Collagen IV, Laminin, and Fibronectin), all marked in red, in lung decellularized scaffolds of control and COPD model groups (400 \times magnification). (C, D) Semiquantitative image analysis of A and B using Image J software. Data are presented as mean \pm standard deviation ($X \pm s$), with * $p < .05$ and *** $p < .001$, $n = 5$.

electron microscopy (SEM) further validated the absence of residual cells and highlighted severe damage to the ultrastructural network in the COPD model group, characterized by enlarged alveolar spaces and reduced alveolar septal thickness. These morphological changes may lead to reduced alveolar elasticity and decreased gas

exchange efficiency, which are closely associated with the dyspnea commonly observed in COPD patients.³¹ These observations indicate that the pathological process of COPD is accompanied by marked tissue remodeling, which may be closely associated with its complex pathophysiological mechanisms, such as chronic

TABLE 3 The proportion of different components of ECM in lung decellularized scaffold of mice in the control group and COPD model group components measurements of collagen fibers (%), elastic fiber (%), and glycosaminoglycan (%) were performed in each group.

Group	Collagen fibers (%)	Elastic fiber (%)	Glycosaminoglycan (%)
Control	16.22 ± 2.52	24.12 ± 2.01	37.66 ± 2.94
COPD	26.95 ± 3.23*	7.46 ± 1.41*	11.04 ± 0.79*

* $p < .05$ versus control group ($n = 5$).

TABLE 4 Average fluorescence intensity of four ECM proteins in the lung decellularized scaffold in the control group and COPD model group Average fluorescence intensity of Collagen I, Collagen IV, Laminin, and Fibronectin was performed in each group.

Group	Collagen I	Collagen IV	Laminin	Fibronectin
Control	4.12 ± 0.37	9.11 ± 1.06	9.14 ± 0.62	5.12 ± 0.46
COPD	12.63 ± 0.86*	22.49 ± 1.47*	18.15 ± 0.77*	7.64 ± 0.16*

* $p < .05$ versus control group ($n = 5$).

inflammation and oxidative stress,^{32,33} as well as cellular senescence and apoptosis.³⁴ These findings not only support existing theories regarding tissue dysfunction and remodeling during COPD progression³⁵ but also provide critical insights for further exploration of the disease's pathological mechanisms and the development of novel therapeutic targets.

The compositional changes in the lung decellularized scaffolds between the COPD model group and the control group were assessed using various staining techniques, including proteoglycans (PGs), glycosaminoglycans (GAGs), collagen, and elastin.³⁶ The results demonstrated that the ECM of COPD lungs exhibited disrupted elastic fiber structures, with significant elastin damage. Collagen, the predominant component of lung ECM,³⁷ showed a disorganized arrangement and localized accumulation in COPD, particularly with notable increases in type I and IV collagen levels. This may be associated with the absence of core proteoglycans and elevated levels of TGF- β .³⁸⁻⁴¹ Elastin damage and abnormal collagen deposition can lead to reduced lung tissue compliance, impairing both ventilation and gas exchange functions of the lung.³⁵ Moreover, the levels of fibronectin (FN) and laminin (LN) were increased in the COPD model group, potentially facilitating the proliferation of fibroblasts and epithelial cells and enhancing immune cell function, thereby altering inflammation or repair processes in COPD patients.^{42,43} The significant reduction in glycosaminoglycan levels could affect the mechanical properties of lung tissue and its ability to inhibit neutrophil elastase, thereby further exacerbating lung tissue damage.^{19,44} These histological and compositional changes are hallmark pathological features of COPD, leading to reduced lung tissue compliance and functional impairment, which in turn contribute to clinical symptoms such as dyspnea and airflow limitation in COPD patients.

This study utilized 4D label-free technology to efficiently screen proteins within lung scaffolds. Compared to the direct proteomic analysis of lung tissue commonly performed in this field,⁴⁵ our study used decellularized lung tissue, eliminating the influence of cellular components and enabling a more accurate understanding of changes in matrix composition. Proteomic analysis identified a total of 3163 proteins, with 70 differentially expressed proteins between the COPD and control groups. GSEA analysis indicated that apoptosis genes were activated in the COPD group, supporting their role in alveolar wall⁴⁶ and pulmonary vascular⁴⁷ damage in COPD. Upregulated proteins, such as Dock9, Smarca2, Rrbp1, Acvr11, and Myl2, and downregulated proteins, such as Ppl, Col6a6, Col6a5, and Myh1, provide insights into the molecular mechanisms underlying COPD pathogenesis.

Collagen formation and degradation were inhibited, notably with significant downregulation of collagen VI precursor proteins Col6a5 and Col6a6. Given the destruction of alveolar wall elastin and collagen fibers in COPD, along with fibroblast-driven collagen deposition, it is reasonable to infer an imbalance in collagen metabolism due to inflammation, oxidative stress, and protease-antiprotease imbalance.^{48,49} Airway remodeling, a key pathological feature of COPD, involves myofibroblasts as crucial effector cells, primarily originating from fibroblast differentiation and epithelial-mesenchymal transition (EMT).⁵⁰ GO and KEGG enrichment analyses revealed significant functional changes between the COPD and control groups. Upregulated proteins were enriched in functions such as carnitine O-acyltransferase activity and regulation of epithelial cell migration, likely related to metabolic adaptations and responses to chronic inflammation. Downregulated proteins were enriched in functions like desmosome, actin filament binding, and cell-cell adhesion, suggesting disruptions in cell-cell interactions and

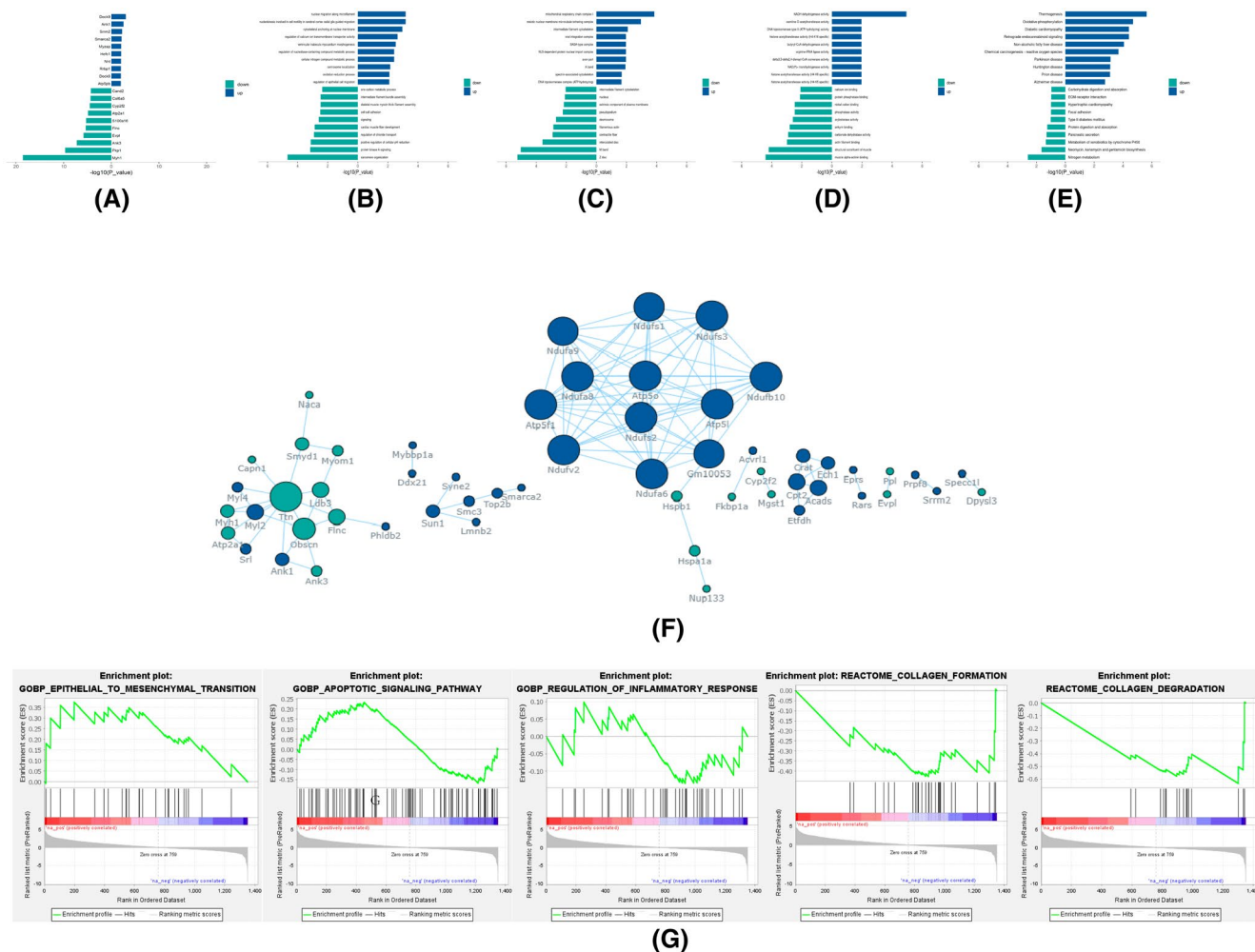


FIGURE 4 Bioinformatics analysis reveals proteomic differences in lung decellularized scaffold. (A) Top 10 Significantly Upregulated and Downregulated Proteins. Compared to the control group, differential expression proteins were screened with a fold change (FC) ≥ 2.0 and $p < .05$ as criteria, and sorted by p -value. The top 10 upregulated and downregulated proteins are listed separately. The color of the bars indicates the direction of expression change: blue for upregulated proteins and cyan for downregulated proteins. (B–D) GO enrichment analysis for upregulated and downregulated proteins. Sorted by FDR (False Discovery Rate), the top 10 significantly enriched GO terms are selected for upregulated and downregulated proteins in (B) Biological Process (BP), (C) Molecular Function (MF), and (D) Cellular Component (CC) categories. The vertical axis represents the names of the GO terms, and the horizontal axis represents the $-\log_{10}$ transformed p -value; the color of the bars represents the change in protein expression, with blue for upregulated proteins and cyan for downregulated proteins; the number behind each bar represents the Rich Factor value, which is the ratio of the proportion of target proteins in a specific GO category to the proportion of total proteins. (E) KEGG pathway enrichment analysis for upregulated and downregulated proteins. Ranked by p -value, the top 10 significantly enriched pathways for both upregulated and downregulated proteins were selected. The vertical axis represents the names of the KEGG pathways, and the horizontal axis represents the $-\log_{10}$ transformed p -value; the color of the bars represents the change in protein expression, with blue indicating upregulated proteins and cyan indicating downregulated proteins; the number following each bar represents the enrichment factor value, which is the ratio of the proportion of target proteins in a specific KEGG pathway to the proportion of all identified proteins in both groups found in that KEGG pathway. (F) Direct Interaction Network Analysis of Differentially Expressed Proteins. In the network, the size of the node is indicative of its degree value; the larger the node, the higher its degree value. (G) GSEA Analysis of Differentially Expressed Proteins.

tissue integrity. KEGG pathway analysis identified significant enrichment in pathways such as focal adhesion and ECM–receptor interaction among the downregulated proteins, indicating potential roles in structural and functional lung tissue alterations. GSEA further suggested that upregulation of genes involved in EMT and apoptosis

contributes to progressive remodeling and cell death in COPD. For example, *Acvr1l* expression was significantly increased in the COPD group. *Acvr1l* encodes a type I cell surface receptor for TGF- β superfamily ligands, promoting smooth muscle actin expression through the *Acvr1l*/*Smad1* axis, which regulates fibroblast differentiation into

myofibroblasts, driving ECM deposition, tissue fibrosis, and airway remodeling.^{51–53} This process is closely associated with airflow limitation in COPD patients, suggesting that *Acvr11* may serve as a potential therapeutic target. Inhibiting its activity could potentially alleviate airway remodeling and improve respiratory function in patients. Additionally, the upregulation of *Myl2* suggests that its phosphorylation enhances airway smooth muscle cell contractile force,⁵⁰ contributing to airway remodeling by promoting fibroblast contraction and migration.⁵⁴ Targeting *Myl2* may help alleviate excessive smooth muscle contraction and improve respiratory function. The upregulation of *Smarca2* and *Skt* proteins indicates their potential involvement in EMT.^{55,56} Inhibiting their activity may reduce EMT and slow the progression of COPD. The study also found decreased expression of *Ank3* (*AnkG*) in the COPD group, suggesting a loss of airway epithelial cell polarity associated with COPD.^{57,58} Restoring *Ank3* expression may help improve epithelial barrier function. Key hub proteins identified in the protein–protein interaction (PPI) network, such as *Ndufs2*, *Ndufa9*, *Acads*, *Myl2*, *Ttn*, *Obscn*, *Ldb3*, and *Myh1*, may play crucial roles in COPD pathophysiology. These proteins are involved in energy metabolism, muscle contraction, and structural maintenance, highlighting the multifaceted nature of the disease. The identification of key proteins provides a new perspective for studying the pathological mechanisms of COPD and lays an important theoretical foundation for developing novel therapeutic targets.

This study elucidates the pathological mechanisms of COPD and identifies potential therapeutic targets; however, certain limitations remain. While proteomic analysis identified key proteins, their functional mechanisms have yet to be fully clarified. Additionally, research based on the decellularized scaffold model lacks *in vivo* validation, making it difficult to fully replicate the complex pathological environment of COPD. Future studies will focus on *in vivo* validation of key protein functions and further exploration of the role of the ECM in cellular function to develop more precise therapeutic strategies for COPD. This study systematically characterizes the morphological, compositional, and proteomic features of COPD lung decellularized scaffolds, providing new insights into the pathogenesis of COPD and laying the foundation for developing therapeutic strategies targeting structural and functional alterations in lung tissue.

AUTHOR CONTRIBUTIONS

Lihua Xie was responsible for the study design, experimental guidance, and article revision. Yuan Li, Yingbing Dai, and Xianyang Liu were in charge of the animal experiments. Yuan Li and Ting Jin were also responsible for the bioinformatics analysis. Yuan Li was

responsible for the writing of the article. All authors approved the final version of the manuscript.

ACKNOWLEDGMENTS

This study was supported by grants from the National Natural Science Foundation of China (Grant Nos. 82070048), the Natural Science Foundation of Hunan Province (Number 2023JJ30849), and the Fundamental Research Funds for the Central Universities of Central South University (1053320231385 and 1053320230888).

DISCLOSURES

The authors declare that throughout the conduct of this research, there were no commercial or financial ties that could potentially be construed as conflicts of interest.

DATA AVAILABILITY STATEMENT

The data that support the findings of this study are openly available in the ProteomeXchange Consortium via the PRIDE partner repository with the dataset identifier PXD058944.

ORCID

Yuan Li  <https://orcid.org/0009-0000-7017-1989>

Yingbing Dai  <https://orcid.org/0009-0003-8130-8989>

Ting Jin  <https://orcid.org/0009-0007-7019-4524>

Xianyang Liu  <https://orcid.org/0009-0000-0365-493X>

Lihua Xie  <https://orcid.org/0009-0007-2394-9090>

REFERENCES

1. Singh D, Agusti A, Anzueto A, et al. Global strategy for the diagnosis, management, and prevention of chronic obstructive lung disease: the GOLD science committee report 2019. *Eur Respir J*. 2019;53(5):1900164. doi:10.1183/13993003.00164-2019
2. Vij N, Chandramani-Shivalingappa P, Van Westphal C, Hole R, Bodas M. Cigarette smoke-induced autophagy impairment accelerates lung aging, COPD-emphysema exacerbations and pathogenesis. *Am J Physiol Cell Physiol*. 2018;314:C73–C87.
3. Postma DS, Timens W. Remodeling in asthma and chronic obstructive pulmonary disease. *Proc Am Thorac Soc*. 2006;3:434–439.
4. Raby KL, Michaeloudes C, Tonkin J, Chung KF, Bhavsar PK. Mechanisms of airway epithelial injury and abnormal repair in asthma and COPD. *Front Immunol*. 2023;14:1201658.
5. Burgstaller G, Oehrle B, Gerckens M, White ES, Schiller HB, Eickelberg O. The instructive extracellular matrix of the lung: basic composition and alterations in chronic lung disease. *Eur Respir J*. 2017;50:1601805.
6. White ES. Lung extracellular matrix and fibroblast function. *Ann Am Thorac Soc*. 2015;12(suppl 1):S30–S33.
7. Hynes RO, Naba A. Overview of the matrisome—an inventory of extracellular matrix constituents and functions. *CSH Perspect Biol*. 2012;4:a004903.
8. Hardie WD, Glasser SW, Hagood JS. Emerging concepts in the pathogenesis of lung fibrosis. *Am J Pathol*. 2009;175:3–16.

9. Mutsaers SE, Bishop JE, McGrouther G, Laurent GJ. Mechanisms of tissue repair: from wound healing to fibrosis. *Int J Biochem Cell Biol.* 1997;29:5-17.
10. Wynn TA. Cellular and molecular mechanisms of fibrosis. *J Pathol.* 2008;214:199-210.
11. Schumann DM, Leeming D, Papakonstantinou E, et al. Collagen degradation and formation are elevated in exacerbated COPD compared with stable disease. *Chest.* 2018;154:798-807.
12. Papakonstantinou E, Roth M, Klagas I, Karakiulakis G, Tamm M, Stolz D. COPD exacerbations are associated with proinflammatory degradation of hyaluronic acid. *Chest.* 2015;148:1497-1507.
13. Nonaka PN, Campillo N, Uriarte JJ, et al. Effects of freezing/thawing on the mechanical properties of decellularized lungs. *J Biomed Mater Res A.* 2014;102:413-419.
14. Hedstrom U, Hallgren O, Oberg L, et al. Bronchial extracellular matrix from COPD patients induces altered gene expression in repopulated primary human bronchial epithelial cells. *Sci Rep-UK.* 2018;8:3502.
15. Sokocevic D, Bonenfant NR, Wagner DE, et al. The effect of age and emphysematous and fibrotic injury on the re-cellularization of de-cellularized lungs. *Biomaterials.* 2013;34:3256-3269.
16. Wagner DE, Bonenfant NR, Parsons CS, et al. Comparative decellularization and recellularization of normal versus emphysematous human lungs. *Biomaterials.* 2014;35:3281-3297.
17. He S, Li L, Sun S, Zeng Z, Lu J, Xie L. A novel murine chronic obstructive pulmonary disease model and the pathogenic role of microRNA-21. *Front Physiol.* 2018;9:503.
18. Kurowska-Stolarska M, Stolarski B, Kewin P, et al. IL-33 amplifies the polarization of alternatively activated macrophages that contribute to airway inflammation. *J Immunol.* 2009;183:6469-6477.
19. Voynow JA, Zheng S, Kumarapurugu AB. Glycosaminoglycans as multifunctional anti-elastase and anti-inflammatory drugs in cystic fibrosis lung disease. *Front Pharmacol.* 2020;11:1011.
20. Bornstein P, Sage EH. Matricellular proteins: extracellular modulators of cell function. *Curr Opin Cell Biol.* 2002;14:608-616.
21. Liakouli V, Cipriani P, Di Benedetto P, et al. The role of extracellular matrix components in angiogenesis and fibrosis: possible implication for systemic sclerosis. *Mod Rheumatol.* 2018;28:922-932.
22. Hoffman ET, Uhl FE, Asarian L, et al. Regional and disease specific human lung extracellular matrix composition. *Biomaterials.* 2023;293:121960.
23. Kubo H. Tissue engineering for pulmonary diseases: insights from the laboratory. *Respirology.* 2012;17:445-454.
24. Sullivan DC, Mirmalek-Sani SH, Deegan DB, et al. Decellularization methods of porcine kidneys for whole organ engineering using a high-throughput system. *Biomaterials.* 2012;33:7756-7764.
25. Ren H, Shi X, Tao L, et al. Evaluation of two decellularization methods in the development of a whole-organ decellularized rat liver scaffold. *Liver Int.* 2013;33:448-458.
26. Sabetkish S, Kajbafzadeh AM, Sabetkish N, et al. Whole-organ tissue engineering: decellularization and recellularization of three-dimensional matrix liver scaffolds. *J Biomed Mater Res A.* 2015;103:1498-1508.
27. Song H, Jiang H, Hu W, et al. Cervical extracellular matrix hydrogel optimizes tumor heterogeneity of cervical squamous cell carcinoma organoids. *Sci Adv.* 2024;10:eadi3511.
28. Su J, Satchell SC, Shah RN, Wertheim JA. Kidney decellularized extracellular matrix hydrogels: rheological characterization and human glomerular endothelial cell response to encapsulation. *J Biomed Mater Res A.* 2018;106:2448-2462.
29. Evangelista-Leite D, Carreira A, Nishiyama MY, Gilpin SE, Miglino MA. The molecular mechanisms of extracellular matrix-derived hydrogel therapy in idiopathic pulmonary fibrosis models. *Biomaterials.* 2023;302:122338.
30. Crapo PM, Gilbert TW, Badylak SF. An overview of tissue and whole organ decellularization processes. *Biomaterials.* 2011;32:3233-3243.
31. Rabe KF, Watz H. Chronic obstructive pulmonary disease. *Lancet.* 2017;389:1931-1940.
32. Brusselle GG, Joos GF, Bracke KR. New insights into the immunology of chronic obstructive pulmonary disease. *Lancet.* 2011;378:1015-1026.
33. Rahman I, Adcock IM. Oxidative stress and redox regulation of lung inflammation in COPD. *Eur Respir J.* 2006;28:219-242.
34. Shapiro SD. Evolving concepts in the pathogenesis of chronic obstructive pulmonary disease. *Clin Chest Med.* 2000;21:621-632.
35. Hogg JC, Timens W. The pathology of chronic obstructive pulmonary disease. *Annu Rev Pathol Mech.* 2009;4:435-459.
36. Kuffa P, Pickard JM, Campbell A, et al. Fiber-deficient diet inhibits colitis through the regulation of the niche and metabolism of a gut pathobiont. *Cell Host Microbe.* 2023;31:2007-2022.
37. Fukuda Y, Masuda Y, Ishizaki M, Masugi Y, Ferrans VJ. Morphogenesis of abnormal elastic fibers in lungs of patients with panacinar and centriacinar emphysema. *Hum Pathol.* 1989;20:652-659.
38. Burgess JK, Weckmann M. Matrikines and the lungs. *Pharmacol Ther.* 2012;134:317-337.
39. Tjin G, Xu P, Kable SH, Kable EP, Burgess JK. Quantification of collagen I in airway tissues using second harmonic generation. *J Biomed Opt.* 2014;19:36005.
40. van Straaten JF, Coers W, Noordhoek JA, et al. Proteoglycan changes in the extracellular matrix of lung tissue from patients with pulmonary emphysema. *Mod Pathol.* 1999;12:697-705.
41. Mouawad JE, Sanderson M, Sharma S, et al. Role of extracellular vesicles in the propagation of lung fibrosis in systemic sclerosis. *Arthritis Rheumatol.* 2023;75:2228-2239.
42. Terranova VP, Aumailley M, Sultan LH, Martin GR, Kleinman HK. Regulation of cell attachment and cell number by fibronectin and laminin. *J Cell Physiol.* 1986;127:473-479.
43. Shibayama H, Tagawa S, Hattori H, Inoue R, Katagiri S, Kitani T. Laminin and fibronectin promote the chemotaxis of human malignant plasma cell lines. *Blood.* 1995;86:719-725.
44. Souza-Fernandes AB, Pelosi P, Rocco PR. Bench-to-bedside review: the role of glycosaminoglycans in respiratory disease. *Crit Care.* 2006;10:237.
45. Skerrett-Byrne DA, Bromfield EG, Murray HC, et al. Time-resolved proteomic profiling of cigarette smoke-induced experimental chronic obstructive pulmonary disease. *Respirology.* 2021;26:960-973.
46. Jiang T, Hu W, Zhang S, et al. Fibroblast growth factor 10 attenuates chronic obstructive pulmonary disease by protecting against glycocalyx impairment and endothelial apoptosis. *Respir Res.* 2022;23:269.
47. Zhang XY, Li W, Zhang JR, Li CY, Zhang J, Lv XJ. Roles of sir-tuin family members in chronic obstructive pulmonary disease. *Respir Res.* 2022;23:66.

48. Karakioulaki M, Papakonstantinou E, Stolz D. Extracellular matrix remodelling in COPD. *Eur Respir Rev.* 2020;29:190124.
49. Chang LY, Fan SM, Liao YC, Wang WH, Chen YJ, Lin SJ. Proteomic analysis reveals anti-fibrotic effects of blue light Photobiomodulation on fibroblasts. *Laser Surg Med.* 2020;52:358-372.
50. Carthy JM. TGFbeta signaling and the control of myofibroblast differentiation: implications for chronic inflammatory disorders. *J Cell Physiol.* 2018;233:98-106.
51. Guida G, Riccio AM. Immune induction of airway remodeling. *Semin Immunol.* 2019;46:101346.
52. Jendzjowsky NG, Kelly MM. The role of airway myofibroblasts in asthma. *Chest.* 2019;156:1254-1267.
53. Schwartze JT, Becker S, Sakkas E, et al. Glucocorticoids recruit Tgfbr3 and Smad1 to shift transforming growth factor-beta signaling from the Tgfbr1/Smad2/3 axis to the Acvrl1/Smad1 axis in lung fibroblasts. *J Biol Chem.* 2014;289:3262-3275.
54. Chen J, Chen J, Tan J, et al. HIF-1alpha dependent RhoA as a novel therapeutic target to regulate rheumatoid arthritis fibroblast-like synoviocytes migration in vitro and in vivo. *J Orthop Transl.* 2023;40:49-57.
55. Wang Y, Li N, Zheng Y, et al. KIAA1217 promotes epithelial-mesenchymal transition and hepatocellular carcinoma metastasis by interacting with and activating STAT3. *Int J Mol sci.* 2021;23(1):104. doi:[10.3390/ijms23010104](https://doi.org/10.3390/ijms23010104)
56. Semba K, Araki K, Li Z, et al. A novel murine gene, sickle tail, linked to the Danforth's short tail locus, is required for normal development of the intervertebral disc. *Genetics.* 2006;172:445-456.
57. Kong C, Qu X, Liu M, et al. Dynamic interactions between E-cadherin and ankyrin-G mediate epithelial cell polarity maintenance. *Nat Commun.* 2023;14:6860.
58. Eapen MS, Sharma P, Gaikwad AV, et al. Epithelial-mesenchymal transition is driven by transcriptional and post transcriptional modulations in COPD: implications for disease progression and new therapeutics. *Int J Chron Obstr Pulm Dis.* 2019;14:1603-1610.

SUPPORTING INFORMATION

Additional supporting information can be found online in the Supporting Information section at the end of this article.

How to cite this article: Li Y, Dai Y, Jin T, Liu X, Xie L. Study on the changes of extracellular matrix morphology and components in COPD animal model by using lung decellularized scaffold. *The FASEB Journal.* 2025;39:e70463. doi:[10.1096/fj.202401522RR](https://doi.org/10.1096/fj.202401522RR)